RESOLUTION ENHANCEMENT FOR HYPERSPECTRAL IMAGES: A SUPER-RESOLUTION AND FUSION APPROACH

Chiman Kwan[†]*, Joon Hee Choi*[‡]*, Stanley Chan*[‡]*, Jin Zhou*[⋆]*, and Bence Budavari*[†]

[†]Signal Processing, Inc., Rockville, MD 20850 USA
[‡]Purdue University, West Lafayette, IN 47907 USA
[⋆]Google, Inc., Mountain View, CA 80305 USA

ABSTRACT

Many remote sensing applications require a high-resolution hyperspectral image. However, resolutions of most hyperspectral imagers are limited to tens of meters. Existing resolution enhancement techniques either acquire additional multispectral band images or use a pan band image. The former poses hardware challenges, whereas the latter has limited performance. In this paper, we present a new resolution enhancement method that only requires a color image. Our approach integrates two newly developed techniques in the area: (1) A hybrid color mapping algorithm, and (2) A Plug-and-Play algorithm for single image super-resolution. Comprehensive experiments using real hyperspectral images are conducted to validate and evaluate the proposed method.

***Index Terms*—** Hyperspectral Imaging, Remote Sensing, Hybrid Color Mapping, Plug-and-Play ADMM, Super-resolution

1. INTRODUCTION

1.1. Motivation

The Hyperspectral Infrared Imager (HyspIRI) is a future mission in NASA to provide global image coverage with potential applications in detecting changes, identifying anomaly and assessing damages due to flooding, hurricane and earthquake [1, 2]. HyspIRI imager offers a 60-meter resolution, typically enough for these applications. However, for more specific applications such as crop monitoring or mineral mapping, the 60-meter resolution remains too coarse.

This paper presents a new resolution enhancement method that improves the resolution by injecting information from high-resolution color images acquired by other types of imagers, such as satellite or airborne image sensors, to the low-resolution hyperspectral image. Color images are becoming less difficult to obtain nowadays, e.g., Google Map's color images can achieve 0.5-meter resolution. However, as we will discuss in the paper, existing fusion techniques are inadequate in producing good quality images because the hyperspectral images suffer from serious blurs. To overcome this challenge, we integrates image deblurring/super-resolution with a fusion algorithm. The new method demonstrates superior performance compared to existing methods.

1.2. Related Work and Proposed Method

Hyperspectral image fusion (or pansharpening) is a known technique in the hyperspectral imaging literature. In a recent report of Loncan et al. [3], the authors made a comprehensive comparison between more than ten fusion methods for hyperspectral images. The following is a short summary of these methods.

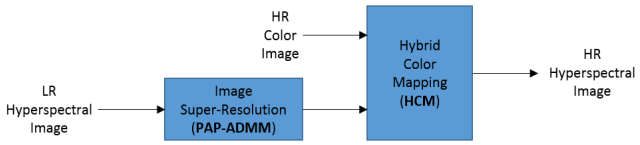

Fig. 1. Outline of the proposed method. We use hybrid color mapping (HCM) to fuse low-resolution (LR) and high-resolution (HR) images. For LR images, we use a single-image super-resolution algorithm to first enhance the resolution before feeding to the HCM.

- Group 1 [4–6]: This group of methods fuse the low-resolution hyperspectral images with high-resolution *multispectral bands* images acquired by other imagers. While they produce good results, they pose many hardware challenges and require knowledge about the point spread function (PSF) that causes the blur in the low-resolution hyperspectral images.
- Group 2 [3, 7–16]: This group of methods fuse the low-resolution hyperspectral images with a high-resolution image in the *panchromatic (pan) band*. Unlike Group 1 methods which require multiple bands, Group 2 only requires the high-resolution pan band but performs worse than Group 1. The other difference is that Group 2 methods do not require the knowledge about the point spread function.

Our proposed method consists of two components as shown in Figure 1. The first component is a middle ground solution of Group 1 and Group 2. Instead of using multispectral bands or just the pan band, we consider a hybrid color mapping (HCM) algorithm [17] that fuses a high-resolution color image with a low-resolution hyperspectral image. The second component is the integration of a single image super-resolution algorithm. Single image super-resolution is a well-studied method in the image processing literature, e.g., [18, 19]. The idea is to up-sample a low-resolution image by using internal image statistics. Our proposed method super-resolves the low-resolution hyperspectral images and then fuses the result using the hybrid color mapping algorithm.

1.3. Scope and Contributions

Besides presenting the proposed algorithm, we are also interested in addressing the following three questions.

Q1. Will a single-image super-resolution alone be sufficient to produce a good high-resolution image? If so, then there is no need for other fusion algorithms. In Section 3.2 we provide a negative answer to this question and show that a single-image super-resolution alone is insufficient.

Q2. How much will the single-image super-resolution improve the HCM algorithm? As reported in [17], the HCM already has a comparable performance to Group 1 and it does not require a PSF. Thus, if the PSF is included, we might be able to obtain even better results. In Section 3.2 we will provide evidence to support this claim.

Q3. Will a single-image super-resolution algorithm help improve Group 2's performance? If the answer is positive, then we do not need the HCM algorithm. However, in Section 3.3, we will show that HCM is needed.

The rest of the paper is organized as follows. We present the proposed algorithm Section II. The experimental results are shown in Section III. Discussions and conclusions are given in Section IV.

2. PROPOSED ALGORITHM

Throughout this paper, we use $\boldsymbol{C} \in \mathbb{R}^{N\times 3}$ to denote a color image of N pixels, and $\boldsymbol{S} \in \mathbb{R}^{N\times P}$ to denote a hyperspectral image of N pixels and P bands. The i-th row of $\boldsymbol{C}$ (and $\boldsymbol{S}$) is the i-th pixel of the color (and hyperspectral) image, and is denoted by $\boldsymbol{c}^i \in \mathbb{R}^{3\times 1}$ (and $\boldsymbol{s}^i \in \mathbb{R}^{P\times 1}$). The j-th column of $\boldsymbol{C}$ (and $\boldsymbol{S}$) is the j-th band of the color (and hyperspectral) image, and is denoted by $\boldsymbol{c}_j \in \mathbb{R}^{N\times 1}$ (and $\boldsymbol{s}_j \in \mathbb{R}^{N\times 1}$). To differentiate the high-resolution and low-resolution images, we put subscripts H and L to write $\boldsymbol{C}_H$ and $\boldsymbol{C}_L$ for color images, and $\boldsymbol{S}_H$ and $\boldsymbol{S}_L$ for hyperspectral images. The number of pixels in a low-resolution image is N and that of a high-resolution image is M. The oversampling factor is defined as $K \stackrel{\text{def}}{=} N/M$. We assume that all images have been registered/aligned. Readers interested in image registration can refer to, e.g., [20, 21].

2.1. Hybrid Color Mapping

Consider a low-resolution color pixel $\boldsymbol{c}^i \in \mathbb{R}^{3\times 1}$ and a low-resolution hyperspectral pixel $\boldsymbol{s}^i \in \mathbb{R}^{P\times 1}$, we define the color mapping as a process to determine a linear transformation $\boldsymbol{T} \in \mathbb{R}^{P\times 3}$ such that

$$\boldsymbol{T} = \underset{\boldsymbol{T}}{\operatorname{argmin}} \sum_{i=1}^{N} \|\boldsymbol{s}^i - \boldsymbol{T}\boldsymbol{c}^i\|_2^2, \tag{1}$$

of which the solution is given by Lemma 1.

Lemma 1. *The solution of* (1) *is*

$$\boldsymbol{T} = \boldsymbol{S}_L\boldsymbol{C}_L^T(\boldsymbol{C}_L\boldsymbol{C}_L^T)^{-1}, \tag{2}$$

where $\boldsymbol{C}_L = [\boldsymbol{c}^1, \ldots, \boldsymbol{c}^N]$ *and* $\boldsymbol{S}_L = [\boldsymbol{s}^1, \ldots, \boldsymbol{s}^N]$.

The minimization in (1) is generally well-posed because $N \gg P$. In practice, the low-resolution color image $\boldsymbol{C}_L$ can be down-sampled from $\boldsymbol{C}_H$ which is assumed given.

A limitation of the color mapping in (1) is that the wavelengths of the color bands only overlap partially with the hyperspectral bands: Color bands covers 0.475μm, 0.51μm, and 0.65μm, whereas hyperspectral bands cover 0.4μm to 2.5μm. The long wavelengths in the hyperspectral bands are not covered by the color bands.

The hybrid color mapping mitigates the problem by preserving the higher bands in the hyperspectral image. Specifically, we select a subset of hyperspectral bands $\{j_1, \ldots, j_k\} \subseteq \{1, \ldots, P\}$ and define

$$\boldsymbol{x}^i = [c_1^i, c_2^i, c_3^i, s_{j_1}^i, \ldots, s_{j_k}^i, 1]^T, \tag{3}$$

where $s_{j_k}^i$ is the i-th pixel of the j_k-th band of the hyperspectral image. Note that we also include the white pixel 1 to adjust for the DC offset due to the atmospheric effects. The hybrid linear transformation $\widetilde{\boldsymbol{T}} \in \mathbb{R}^{P\times(4+k)}$ is therefore

$$\widetilde{\boldsymbol{T}} = \underset{\widetilde{\boldsymbol{T}}}{\operatorname{argmin}} \sum_{i=1}^{N} \|\boldsymbol{s}^i - \widetilde{\boldsymbol{T}}\boldsymbol{x}^i\|_2^2, \tag{4}$$

whose solution has the same form as Lemma 1.

Remark: For further improvement of the hybrid color mapping, we can divide the image into overlapping patches where each patch has its own $\boldsymbol{T}$. This tends to improve the performance of the algorithm significantly.

Once the transformation $\boldsymbol{T}$ is obtained, the high-resolution hyperspectral image $\boldsymbol{S}_H$ can be reconstructed by

$$\boldsymbol{S}_H = \boldsymbol{T}\boldsymbol{C}_H, \tag{5}$$

where $\boldsymbol{C}_H$ is the given high-resolution color image. The reconstruction of $\boldsymbol{S}_H$ using $\widetilde{\boldsymbol{T}}$ is more challenging because we need the bands $s_{j_1}^i, \ldots, s_{j_k}^i$ from the high-resolution image which is not yet available. This leads to our next component using single-image super-resolution.

2.2. Plug-and-Play ADMM

Plug-and-Play ADMM (PAP-ADMM) is a generic optimization algorithm for image restoration problems [19, 22]. For the purpose of this paper, we describe PAP-ADMM for recovering high-resolution images from the low-resolution observations.

Consider the j-th band of the hyperspectral image $\boldsymbol{s}_j$. We denote $\boldsymbol{s}_j^H \in \mathbb{R}^{M\times 1}$ the high-resolution version of $\boldsymbol{s}_j$ and $\boldsymbol{s}_j^L \in \mathbb{R}^{N\times 1}$ the low-resolution version of $\boldsymbol{s}_j$. These two resolutions are related by

$$\boldsymbol{s}_j^L = \boldsymbol{D}\boldsymbol{A}\boldsymbol{s}_j^H + \boldsymbol{\eta}, \tag{6}$$

where $\boldsymbol{A} \in \mathbb{R}^{M\times M}$ is a convolution matrix representing the blur (i.e., the point spread function), $\boldsymbol{D} \in \mathbb{R}^{N\times M}$ is a down-sampling matrix, and $\boldsymbol{\eta} \sim \mathcal{N}(0, \sigma^2)$ is an i.i.d. Gaussian noise vector. The problem of image super-resolution is to solve an optimization

$$(\boldsymbol{s}_1^H, \ldots, \boldsymbol{s}_P^H) = \underset{\boldsymbol{s}_1^H,\ldots,\boldsymbol{s}_P^H}{\operatorname{argmin}} \sum_{j=1}^{P} \left(\|\boldsymbol{s}_j^L - \boldsymbol{D}\boldsymbol{A}\boldsymbol{s}_j^H\|^2 + \lambda g(\boldsymbol{s}_j^H) \right), \tag{7}$$

for some regularization function $g(\cdot)$ and parameter λ.

The PAP-ADMM algorithm is a variant of the classical ADMM algorithm [23] which replaces the regularization function $g(\cdot)$ by an implicit regularization function in terms of an image denoiser $\mathcal{D}$. Without going into the details of the PAP-ADMM algorithm (which can be found in [19]), we summarize the steps involved as follows. First, we note that (7) is separable and so we can solve each $\boldsymbol{s}_j^H$ individually. For the j-th band, the algorithm updates iteratively the following quantities

$$\begin{aligned}
\boldsymbol{s}_j^H &= \underset{\boldsymbol{s}_j^H}{\operatorname{argmin}} \|\boldsymbol{D}\boldsymbol{A}\boldsymbol{s}_j^H - \boldsymbol{s}_j^L\|^2 + \frac{\rho}{2}\|\boldsymbol{s}_j^H - (\boldsymbol{v}_j - \boldsymbol{u}_j)\|^2 \\
\boldsymbol{v}_j &= \mathcal{D}\left(\boldsymbol{s}_j^H + \boldsymbol{u}_j, \sqrt{\lambda/\rho}\right) \\
\boldsymbol{u}_j &= \boldsymbol{u}_j + (\boldsymbol{s}_j^H - \boldsymbol{v}_j),
\end{aligned}$$

where $\boldsymbol{v}_j$ and $\boldsymbol{u}_j$ are intermediate variables defined by the PAP-ADMM algorithm, and $\mathcal{D}(\cdot, \sigma)$ is an image denoiser which denoises the input argument with a noise level σ. In this paper, the image denoiser we use is BM3D [24], although other denoisers can also be used. The internal parameter ρ is fixed at $\rho = 1$.

3. EXPERIMENTAL RESULTS

In this section we present experimental results along with the conclusions for questions Q1-Q3. We use two hyperspectral image datasets: (1) AF data from the Air Force [25] and (2) AVIRIS data from NASA [26]. The AF image has a size of $267 \times 342 \times 124$, ranging from 461nm to 901nm. The AVIRIS image has a size of $300 \times 300 \times 213$, ranging from 380nm to 2500nm.

To simulate the low-resolution hyperspectral images, we follow [3] by downsampling the images spatially with a factor of $K = 9$ (3×3) using a 5×5 Gaussian point spread function. The color image RGB channels are taken from the appropriate bands of the high-resolution hyperspectral images.

3.1. Evaluation Metric

We evaluate the performance of image reconstruction algorithms using the following metrics.

- **RMSE**. The RMSE of two high-resolution hyperspectral images $\boldsymbol{S} \in \mathbb{R}^{M \times P}$ and $\widehat{\boldsymbol{S}} \in \mathbb{R}^{M \times P}$ is defined as

$$\mathrm{RMSE}(\boldsymbol{S}, \widehat{\boldsymbol{S}}) = \sqrt{\frac{1}{P}\sum_{j=1}^{P}\left(\frac{1}{M}\|\boldsymbol{s}_j - \widehat{\boldsymbol{s}}_j\|_2^2\right)}.$$

- **CC** (Cross-Correlation). The cross-correlation between $\boldsymbol{S}$ and $\widehat{\boldsymbol{S}}$ is defined as

$$\mathrm{CC}(\boldsymbol{S}, \widehat{\boldsymbol{S}}) = \frac{1}{P}\sum_{j=1}^{P}\left(\frac{\sum_{i=1}^{M}(s_j^i - \mu_j)(\widehat{s}_j^i - \widehat{\mu}_j)}{\sqrt{\sum_{i=1}^{M}(s_j^i - \mu_j)^2 \sum_{i=1}^{M}(\widehat{s}_j^i - \widehat{\mu}_j)^2}}\right),$$

  with μ_j and $\widehat{\mu}_j$ being the mean of the vector $\boldsymbol{s}_j$ and $\widehat{\boldsymbol{s}}_j$.

- **SAM** (Spectral Angle Mapper). The spectral angle mapper is

$$\mathrm{SAM}(\boldsymbol{S}, \widehat{\boldsymbol{S}}) = \frac{1}{M}\sum_{i=1}^{M}\left(\cos^{-1}\left\{\frac{\langle \boldsymbol{s}^i, \widehat{\boldsymbol{s}}^i\rangle}{\|\boldsymbol{s}^i\|_2\|\widehat{\boldsymbol{s}}^i\|_2}\right\}\right).$$

- **ERGAS** (Erreur Relative. Globale Adimensionnelle de Synthese). The ERGAS is defined as

$$\mathrm{ERGAS}(\boldsymbol{S}, \widehat{\boldsymbol{S}}) = 100d\sqrt{\frac{1}{P}\sum_{j=1}^{P}\left(\frac{\mathrm{RMSE}_j}{\mu_j}\right)^2},$$

  for some constant d depending on the resolution.

3.2. Comparison between HCM and PAP-ADMM

This experiment aims to address the question of why we need both hybrid color mapping and the Plug-and-Play ADMM. The result is shown in Table 1 and Figure 2, where we observe that the integrated approach "PAP-ADMM + HCM" achieves the best performance overall. Such result is not surprising, because PAP-ADMM alone does not utilize the rich information in the color band, whereas the HCM method without an appropriate high-resolution input does not generate a good transformation $\boldsymbol{T}$. This answers Q1 and Q2.

We should also point out an interesting observation if we look at the RMSE of individual bands. As shown in Figure 3, the proposed algorithm actually performs well for lower bands such as the visible and the near infrared bands. However, for higher bands such as the short wave infrared, PAP-ADMM alone produces the best result. A reason to this is that the color band has diminishing correlation to the spectral bands as we move to higher bands.

Methods	RMSE	CC	SAM	ERGA
PAP-ADMM [19]	66.2481	**0.9889**	0.9889	1.9783
HCM [17]	44.3475	0.9492	0.9906	2.0302
PAP-ADMM + HCM	**31.7023**	0.9563	**0.9169**	**1.8953**

Table 1. Comparison of variant methods of HCM and PAP-ADMM on AVIRIS.

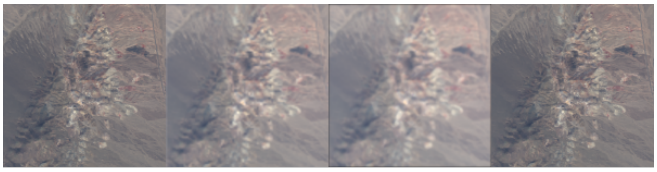

Fig. 2. AVIRIS images in visible range using different methods

3.3. Comparison with Group 2 Methods

We compare the proposed algorithm with Group 2 methods. Since our proposed method assumes knowledge about the point spread function and a specific image super-resolution algorithm, for fair comparison we down-sample the PAP-ADMM results to simulate a deblurred but down-sampled hyperspectral image. Then, we feed the results to Group 2 methods to see if Group 2 methods are improved.

The result of this experiment is shown in Table 2. As we can see, the performance of Group 2 is actually detrimental. One reason is that Group 2 methods are already injecting high frequency contents into the hyperspectral images through the pan band. This can be seen from the general formulation of Group 2 methods:

$$\boldsymbol{s}_j^H = \mathcal{B}(\boldsymbol{s}_j^L) + \alpha(\boldsymbol{s}_{\mathrm{pan}}^H - \widetilde{\boldsymbol{s}}_{\mathrm{pan}}^H), \tag{8}$$

where $\mathcal{B}(\cdot)$ is the bicubic interpolation, α is a gain factor, $\boldsymbol{s}_{\mathrm{pan}}^H$ is the high-resolution pan-band image, and $\widetilde{\boldsymbol{s}}_{\mathrm{pan}}^H$ is a lowpassed high-resolution pan-band image. The pan-band in this experiment is the average of the 3 color bands from the input image for both the AF and AVIRIS datasets. The reason why Group 2 methods do not benefit from PAP-ADMM is that the residue $(\boldsymbol{s}_{\mathrm{pan}}^H - \widetilde{\boldsymbol{s}}_{\mathrm{pan}}^H)$ is the high-frequency content injected by the pan-band. An extra deblurring step on these Group 2 results tend to overcompensate the effects. Therefore, having a strong super-resolution step for Group 2 does not help, and this answers Q3.

In contrast to Group 2 methods, the proposed HCM method benefits significantly from the PAP-ADMM step. One reason is that HCM is using $\boldsymbol{T}$ to generate the high-resolution image and no explicit high frequency contents are injected yet. This finding also validates the importance of both HCM and the PAP-ADMM.

3.4. Comparison with Group 1

We finally compare the performance of the proposed algorithm with Group 1 methods. Table 2 shows the results. The average RMSE of our method is very close to that of Bayes Sparse for the AF data and much better for the AVIRIS data. However, if we inspect closely at Figure 3, we see that our method actually has lower RMSE for majority of the low bands. Moreover, if we look at the AVIRIS's RMSE in Figure 3, we observe that even at higher bands our performance is comparable to Group 1. The performance in AF's CC plot is even more dramatic. Therefore, if multispectral images could be used, our proposed method can possibly achieve even better results.

		AF					AVIRIS				
Group	**Methods**	Time	RMSE	CC	SAM	ERGAS	Time	RMSE	CC	SAM	ERGAS
1	CNMF [4]	12.52	0.5992	0.9922	1.4351	1.7229	23.75	32.2868	0.9456	0.9590	2.1225
	Bayes Naive [5]	0.58	0.4357	0.9881	1.2141	1.6588	0.86	67.2879	0.9474	0.8136	2.1078
	Bayes Sparse [6]	208.82	**0.4133**	0.9900	1.2395	1.5529	235.50	51.7010	0.9619	**0.7635**	1.8657
2	SFIM [16]	0.99†	0.7176	0.9846	1.5014	2.2252	1.56†	63.7443	0.9469	0.9317	2.0790
	MTF GLP [12]	1.38†	0.8220	0.9829	1.6173	2.4702	2.25†	57.5260	0.9524	0.9254	2.0103
	MTF GLP HTM [13]	1.40†	0.8096	0.9833	1.5540	2.4387	2.23†	57.5618	0.9524	0.9201	2.0119
	GS [10]	1.05†	2.1787	0.8578	2.4462	7.0827	1.83†	54.9411	0.9554	0.9420	1.9609
	GSA [11]	1.21†	0.7485	0.9875	1.5212	2.1898	1.98†	32.4501	**0.9695**	0.8608	**1.6660**
	PCA [8]	2.37†	2.3819	0.8382	2.6398	7.7194	2.98†	48.9916	0.9603	0.9246	1.8706
	GFPCA [9]	1.17†	0.6478	0.9862	1.5370	2.0573	2.17†	61.9038	0.9391	1.1720	2.2480
	Hysure [14, 15]	117.06†	0.8683	0.9810	1.7741	2.6102	62.47†	38.8667	0.9590	1.0240	1.8667
3	PAP-ADMM [19]	2144.00	0.4308	0.9889	1.1622	1.6149	3368.00	66.2481	0.9531	0.7848	1.9783
	Super Resolution [18]	279.18	0.5232	0.9839	1.3215	1.9584	1329.59	86.7154	0.9263	0.9970	2.4110
	Bicubic [27]	**0.04**	0.5852	0.9807	1.3554	2.1560	**0.10**	92.2143	0.9118	1.0369	2.5728
Ours	HCM no deblur [17]	0.59	0.5812	0.9908	1.4223	1.7510	1.50	44.3475	0.9492	0.9906	2.0302
	HCM+Lucy [28]	1.02	0.6009	0.9879	1.3950	1.9308	1.50	37.2436	0.9518	0.9683	1.9720
	Our method	0.59†	0.4151	**0.9956**	**1.1442**	**1.2514**	1.50†	**30.1907**	0.9672	0.9008	1.7205

Table 2. Comparison of our methods with various pansharpening methods on AF and AVIRIS. †: These methods involve PAP-ADMM but we did not include PAP-ADMM's runtime in order to illustrate the differences.

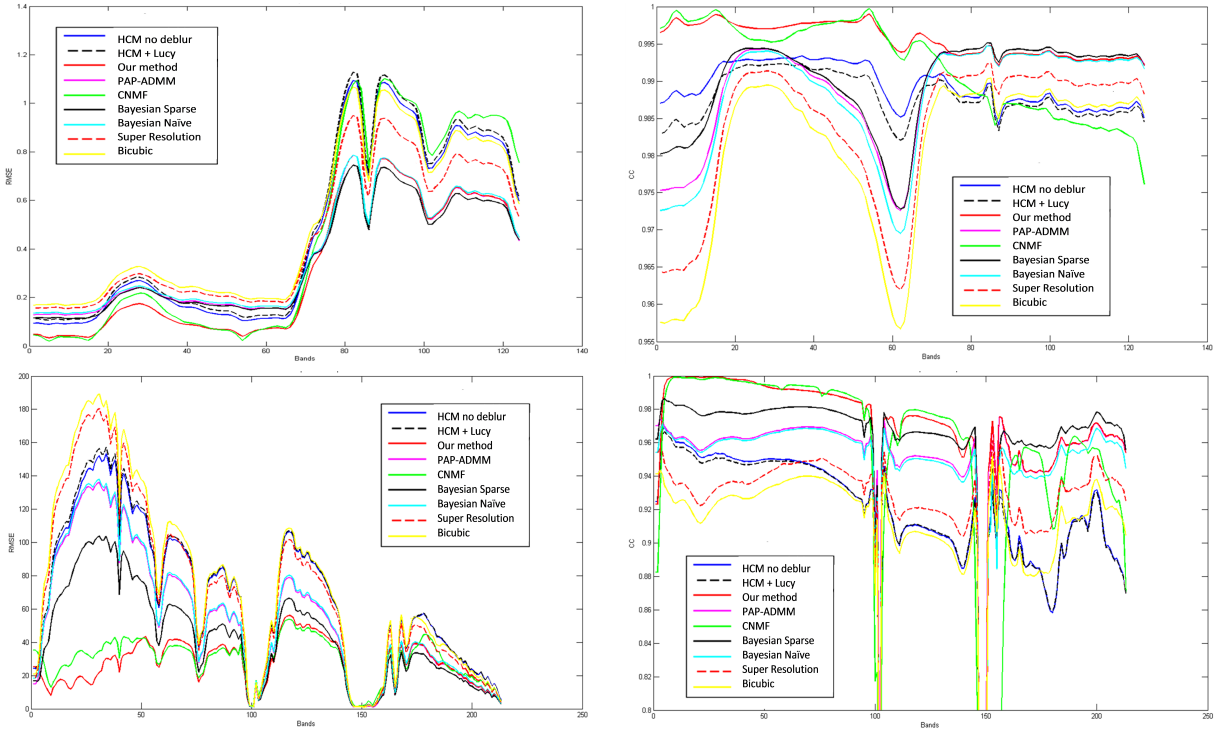

Fig. 3. Comparison of RMSE and CC between our method and methods in Groups 1 and 3 on AF(left) and AVIRIS (right).

3.5. Runtime

The runtime of our proposed method is slower than Group 1 methods because the current PAP-ADMM is a frame-by-frame algorithm. We believe that the runtime can be significantly reduced if we use faster denoisers than BM3D and exploit the correlation across different bands. Future work will be focused on the speed up.

4. CONCLUSION

We presented a new fusion based image processing algorithm to enhance the resolution of hyperspectral images. Our new algorithm is an integration of a hybrid color mapping algorithm and a single-image super-resolution algorithm. While the concept of the new approach is simple, the performance is promising as we compare to existing algorithms on real image datasets. Future research direction will be focused on speeding up the algorithm, and investigating the performance gain in classification and other high-level vision tasks.

Acknowledgment. Technical discussions with Ms. L. Loncan and Dr. Q. Wei related to the codes in [3] were tremendously helpful in running our simulations. We also would like to thank the authors of [18] for sharing their source codes with us.

5. REFERENCES

[1] R. O. Green, G. Asner, S. Ungar, and R. Knox, "Nasa mission to measure global plant physiology and functional types," in *IEEE Aerospace Conference*, Mar 2008, pp. 1–7.

[2] C. M. Lee, M. L. Cable, S. J. Hook, R. O. Green, S. L. Ustin, D. J. Mandl, and E. M. Middleton, "An introduction to the nasa hyperspectral infrared imager (hyspiri) mission and preparatory activities," *Remote Sensing of Environment*, vol. 167, pp. 6–19, Sept. 2015.

[3] L. Loncan, L. B. de Almeida, J. M. Bioucas-Dias, X. Briottet, J. Chanussot, N. Dobigeon, S. Fabre, W. Liao, G. A. Licciardi, M. Simoes, J. Y. Tourneret, M. A. Veganzones, G. Vivone, Q. Wei, and N. Yokoya, "Hyperspectral pansharpening: A review," *IEEE Geoscience and Remote Sensing Magazine*, vol. 3, no. 3, pp. 27–46, Sept. 2015.

[4] N. Yokoya, T. Yairi, and A. Iwasaki, "Coupled nonnegative matrix factorization unmixing for hyperspectral and multispectral data fusion," *IEEE Transactions on Geoscience and Remote Sensing*, vol. 50, no. 2, pp. 528–537, Feb. 2012.

[5] R. C. Hardie, M. T. Eismann, and G. L. Wilson, "Map estimation for hyperspectral image resolution enhancement using an auxiliary sensor," *IEEE Transactions on Image Processing*, vol. 13, no. 9, pp. 1174–1184, Sept. 2004.

[6] Q. Wei, J. Bioucas-Dias, N. Dobigeon, and J. Y. Tourneret, "Hyperspectral and multispectral image fusion based on a sparse representation," *IEEE Transactions on Geoscience and Remote Sensing*, vol. 53, no. 7, pp. 3658–3668, Jul 2015.

[7] M. Moller, T. Wittman, A. L. Bertozzi, and M. Burger, "A variational approach for sharpening high dimensional images," *SIAM Journal on Imaging Sciences*, vol. 5, no. 1, pp. 150–178, 2012.

[8] P. S. Chavez Jr., S. C. Sides, and J. A. Anderson, "Comparison of three different methods to merge multiresolution and multispectral data: Landsat tm and spot panchromatic," *Photogrammetric Engineering & Remote Sensing*, vol. 57, no. 3, pp. 295–303, March 1991.

[9] W. Liao, X. Huang, F. V. Coillie, S. Gautama, A. Pizurica, W. Philips, H. Liu, T. Zhu, M. Shimoni, G. Moser, and D. Tuia, "Processing of multiresolution thermal hyperspectral and digital color data: Outcome of the 2014 ieee grss data fusion contest," *IEEE Journal of Selected Topics in Applied Earth Observations and Remote Sensing*, vol. 8, no. 6, pp. 2984–2996, Jun 2015.

[10] C. Laben and B. Brower, "Process for enhancing the spatial resolution of multispectral imagery using pan-sharpening," Jan 2000, US Patent 6011875.

[11] B. Aiazzi, S. Baronti, and M. Selva, "Improving component substitution pansharpening through multivariate regression of ms+pan data," *IEEE Transactions on Geoscience and Remote Sensing*, vol. 45, no. 10, pp. 3230–3239, Oct. 2007.

[12] B. Aiazzi, L. Alparone, S. Baronti, A. Garzelli, and M. Selva, "Mtf-tailored multiscale fusion of high-resolution ms and pan imagery," *Photogrammetric Engineering & Remote Sensing*, vol. 72, no. 5, pp. 591–596, May 2006.

[13] G. Vivone, R. Restaino, M. Dalla Mura, G. Licciardi, and J. Chanussot, "Contrast and error-based fusion schemes for multispectral image pansharpening," *IEEE Geoscience and Remote Sensing Letters*, vol. 11, no. 5, pp. 930–934, May 2014.

[14] M. Simoes, J. Bioucas-Dias, L. B. Almeida, and J. Chanussot, "A convex formulation for hyperspectral image superresolution via subspace-based regularization," *IEEE Transactions on Geoscience and Remote Sensing*, vol. 53, no. 6, pp. 3373–3388, June 2015.

[15] M. Simoes, J. Bioucas-Dias, L. B. Almeida, and J. Chanussot, "Hyperspectral image superresolution: An edge-preserving convex formulation," in *2014 IEEE International Conference on Image Processing (ICIP)*, Oct. 2014, pp. 4166–4170.

[16] J. G. Liu, "Smoothing filter based intensity modulation: A spectral preserve image fusion technique for improving spatial details," *International Journal of Remote Sensing*, vol. 21, no. 18, pp. 3461–3472, Dec. 2000.

[17] J. Zhou, C. Kwan, and B. Budavari, "Hyperspectral image super-resolution: A hybrid color mapping approach," *Journal of Applied Remote Sensing*, vol. 10, no. 3, pp. 035024, Sep 2016.

[18] Qing Yan, Yi Xu, Xiaokang Yang, and Truong Q. Nguyen, "Single image superresolution based on gradient profile sharpness," *IEEE Transactions on Image Processing*, vol. 24, no. 10, pp. 3187–3202, Oct. 2015.

[19] S. H. Chan, X. Wang, and O. A. Elgendy, "Plug-and-play admm for image restoration: Fixed point convergence and applications," *IEEE Transactions on Computational Imaging*, vol. PP, no. 99, pp. 1–1, Nov 2016.

[20] B. K. P. Horn and B. G. Schunck, "Determining optical flow," *Artificial Intelligence*, vol. 17, no. 1-3, pp. 185–203, Aug 1981.

[21] J. L. Barron, D. J. Fleet, and S. S. Beauchemin, "Performance of optical flow techniques," *International Journal of Computer Vision*, vol. 12, no. 1, pp. 43–77, Feb 1994.

[22] S. Sreehari, S. V. Venkatakrishnan, B. Wohlberg, L. F. Drummy, J. P. Simmons, and C. A. Bouman, "Plug-and-play priors for bright field electron tomography and sparse interpolation," to appear in the IEEE Transactions on Computational Imaging, 2016.

[23] S. Boyd, N. Parikh, E. Chu, B. Peleato, and J. Eckstein, "Distributed optimization and statistical learning via the alternating direction method of multipliers," *Found. Trends Mach. Learn.*, vol. 3, no. 1, pp. 1–122, Jan. 2011.

[24] K. Dabov, A. Foi, V. Katkovnik, and K. Egiazarian, "Image denoising by sparse 3–d transform-domain collaborative filtering," *IEEE Transactions on Image Processing*, vol. 16, no. 8, pp. 2080–2095, Aug. 2007.

[25] Q. Du, "A new method for change analysis of multi-temporal hyperspectral images," in *2012 4th Workshop on Hyperspectral Image and Signal Processing: Evolution in Remote Sensing (WHISPERS)*, June 2012, pp. 1–4.

[26] S. J. Hook and M Rast, "Mineralogic mapping using airborne visible infrared imaging spectrometer (aviris), shortwave infrared (swir) data acquired over cuprite, nevada," in *Proceedings of the Second Airborne Visible Infrared Imaging Spectrometer (AVIRIS) Workshop*. 1990, pp. 199–207, JPL Publication.

[27] R. Keys, "Cubic convolution interpolation for digital image processing," *IEEE Transactions on Acoustics, Speech, and Signal Processing*, vol. 29, no. 6, pp. 1153–1160, Dec. 1981.

[28] D. A. Fish, J. G. Walker, A. M. Brinicombe, and E. R. Pike, "Blind deconvolution by means of the richardson-lucy algorithm," *Journal of the Optical Society of America A*, vol. 12, no. 1, pp. 58–65, Jan. 1995.